Construction of 2D/0D/2D Face-to-Face Contact g-C$_3$N$_4$@Au@Bi$_4$Ti$_3$O$_{12}$ Heterojunction Photocatalysts for Degradation of Rhodamine B

HUAJING GAO,[1] XINXIN ZHAO,[1] HAIMIN ZHANG,[1] JIAFU CHEN,[2] SHIFA WANG,[3] and HUA YANG [1,4]

1.—School of Science, Lanzhou University of Technology, Lanzhou 730050, China. 2.—Ministry of Education Key Laboratory of Testing Technology for Manufacturing Process, Southwest University of Science and Technology, Mianyang 621010, China. 3.—School of Electronic and Information Engineering, Chongqing Three Gorges University, Chongqing 404000, Wanzhou, China. 4.—e-mail: hyang@lut.edu.cn

A type of two-dimensional/zero-dimensional/two-dimensional face-to-face contact g-C$_3$N$_4$@Au@Bi$_4$Ti$_3$O$_{12}$ heterojunction ternary composite photocatalyst has been developed by coupling Bi$_4$Ti$_3$O$_{12}$ nanosheets with g-C$_3$N$_4$ nanosheets face-to-face and sandwiching Au nanoparticles between them. The as-prepared photocatalysts were systematically investigated using various characterization techniques including x-ray powder diffraction analysis, ultraviolet–visible diffuse reflectance spectroscopy, Fourier-transform infrared spectroscopy, scanning electron microscopy, transmission electron microscopy, and x-ray photoelectron spectroscopy. Degradation experiments were carried out to study the removal of rhodamine B from water under simulated sunlight, revealing that the g-C$_3$N$_4$@Au@Bi$_4$Ti$_3$O$_{12}$ composite photocatalysts exhibited greatly enhanced photodegradation performance compared with bare Bi$_4$Ti$_3$O$_{12}$ or g-C$_3$N$_4$ nanosheets, and moreover excellent photocatalytic stability during repeated dye degradation with recycling. The underlying photodegradation mechanism of the g-C$_3$N$_4$@Au@Bi$_4$Ti$_3$O$_{12}$ composite photocatalysts was systematically investigated and is discussed herein.

Key words: Bi$_4$Ti$_3$O$_{12}$ nanosheets, g-C$_3$N$_4$ nanosheets, Au nanoparticles, g-C$_3$N$_4$@Au@Bi$_4$Ti$_3$O$_{12}$ heterojunctions, face-to-face contact, photodegradation performance

INTRODUCTION

Water, being an important element for life, is becoming increasingly polluted due to the generation of huge amounts of wastewater annually by chemical industries. Organic dyes, e.g., rhodamine B (RhB), are important constituents of such industrial effluents, representing a potential threat to human health and survival due to their high water solubility, chemical stability, nonbiodegradability, and carcinogenicity. In recent years, semiconductor-based photocatalysis has attracted increasing interest for water remediation.[1–4] This technology stands out due to its ability to use solar radiation to decompose harmful organic dyes. Sunlight-induced conduction-band (CB) electrons (e$^-$) and valence-band (VB) holes (h$^+$) in photocatalysts exhibit reduction/oxidation capabilities as the basic reactive species that take part in direct or indirect redox reactions to cause dye decomposition. Nevertheless, the photodegradation activity of most semiconductor photocatalysts is limited due to the easy recombination of photoexcited e$^-$–h$^+$ pairs. Efficient suppression of photoexcited electron/hole recombination has thus become one of the most important

Construction of 2D/0D/2D Face-to-Face Contact g-C$_3$N$_4$@Au@Bi$_4$Ti$_3$O$_{12}$ Heterojunction
Photocatalysts for Degradation of Rhodamine B

5249

strategies to improve the photodegradation performance of semiconductors.[5–12]

Noble-metal and carbon nanomaterials, which have attracting extensive attention owing to their outstanding physical properties and broad application prospects,[13–21] have been extensively employed to modify photocatalysts to improve their photodegradation performance.[22–27] The main mechanism for such enhancement is that these nanomaterials can serve as good electron sinks to trap photogenerated electrons, thus decreasing the combination of e$^-$–h$^+$ pairs. Furthermore, these nanomaterials can efficiently absorb and utilize visible light during the photocatalytic process, favoring photoluminescence upconversion of carbon nanomaterials and the localized surface plasmon resonance (LSPR) of noble-metal nanoparticles.[28–30] The construction of semiconductor–semiconductor heterojunctions is another important avenue that has shown an ability to separate photoexcited e$^-$/h$^+$ pairs.[31–35] The photogenerated carriers are thereby transferred from one semiconductor to another under the action of the internal electric field formed at the heterojunction interface, resulting in efficient e$^-$–h$^+$ separation. Optimization of the interface and realizing a good contact between the two semiconductors are the key points to facilitate such carrier transfer and separation.

Bismuth titanate (Bi$_4$Ti$_3$O$_{12}$, BTO), with a bandgap energy of $\sim$ 3.1 eV[36] and crystallizing in a layered structure formed by an alternating stack of perovskite-like (Bi$_2$Ti$_3$O$_{10}$)$^{2-}$ blocks and (Bi$_2$O$_2$)$^{2+}$ units, has attracted much attention recently as an important semiconductor photocatalyst for photodegradation of organic pollutants.[37–41] Due to its special layer structure, Bi$_4$Ti$_3$O$_{12}$ exhibits a high anisotropy of photocatalytic properties. In particular, the (010) facet is expected to exhibit high photocatalytic activity because photogenerated electrons and holes are readily separated and migrate to the (010) facet driven by the polarization electric field (along the [010] direction).[42] This effect was confirmed by the observation of an extremely high photodegradation activity for two-dimensional (2D) Bi$_4$Ti$_3$O$_{12}$ nanosheets with nearly 100% exposed (010) facet.[35] Graphite-like carbon nitride (g-C$_3$N$_4$, CN) is well known as a metal-free polymeric semiconductor, showing promising visible-light-responsive photoactivity.[38] Due to its simple preparation and excellent thermal/chemical stability, g-C$_3$N$_4$ is attractive for applications in photodegradation of organic dyes. Moreover, g-C$_3$N$_4$ presents abundant surface groups, indicating its suitability for hybridization with other photocatalysts to form heterojunctions.[43–47]

In the work described herein, g-C$_3$N$_4$ and Bi$_4$Ti$_3$O$_{12}$ nanosheets were coupled together face-to-face via a hydrothermal route. The resulting two-dimensional (2D)/2D g-C$_3$N$_4$@Bi$_4$Ti$_3$O$_{12}$ heterojunctions have a maximum contact area and exhibit favorable carrier transfer and separation.

Furthermore, zero-dimensional (0D) Au nanoparticles were sandwiched between the g-C$_3$N$_4$ and Bi$_4$Ti$_3$O$_{12}$ nanosheets to construct 2D/0D/2D g-C$_3$N$_4$@Au@Bi$_4$Ti$_3$O$_{12}$ heterojunctions, where the Au nanoparticles serve as conductive bridges to facilitate charge transfer between g-C$_3$N$_4$ and Bi$_4$Ti$_3$O$_{12}$. RhB was used as a model dye to evaluate the photocatalysis degradation performance of the as-prepared g-C$_3$N$_4$@Au@Bi$_4$Ti$_3$O$_{12}$ composite photocatalysts under irradiation by simulated sunlight. The results demonstrate that the photodecomposition performance of the composite photocatalysts was much higher than that of bare g-C$_3$N$_4$ or Bi$_4$Ti$_3$O$_{12}$ nanosheets.

EXPERIMENTAL PROCEDURES

Synthesis of g-C$_3$N$_4$ and Bi$_4$Ti$_3$O$_{12}$ Nanosheets

All chemical reagents (of analytical grade) used in the present experiments were supplied directly by chemical companies and used without further purification. Simple pyrolysis of melamine was used to fabricate g-C$_3$N$_4$ nanosheets. Typically, 5 g melamine was placed in a corundum boat, semi-closed with a cover, then calcined in a tube furnace at 520°C for 4 h. The calcined product was ground, finally resulting in g-C$_3$N$_4$ nanosheets.

A hydrothermal method as elaborated in literature was employed to synthesize Bi$_4$Ti$_3$O$_{12}$ nanosheets.[35] A stoichiometric amount of bismuth nitrate pentahydrate [Bi(NO$_3$)$_3$·5H$_2$O, 1.9402 g] was dissolved in 10% (v/v) dilute nitric acid solution. To the Bi(NO$_3$)$_3$ solution was then slowly added titanium tetrachloride solution (0.5691 g TiCl$_4$ + 20 mL deionized water) and sodium hydroxide solution (4.8 g NaOH + 40 mL deionized water). The resulting mixture was loaded into a Teflon-lined autoclave and subjected to hydrothermal reaction at 200°C for 24 h. Thereafter, the precipitate was collected as Bi$_4$Ti$_3$O$_{12}$ nanosheets, then washed with deionized water/absolute ethanol and dried at 60°C for 12 h.

Fabrication of CN@BTO Composites

During the above-described hydrothermal process for preparation of Bi$_4$Ti$_3$O$_{12}$ nanosheets, stoichiometric g-C$_3$N$_4$ nanosheets were uniformly dispersed in the precursor mixture solution, resulting in the preparation of CN@BTO composites. The hydrothermal reaction and sample collection/washing/drying process were performed under constant temperature/time conditions. By adding different amounts of g-C$_3$N$_4$ nanosheets in the precursor mixture solution, several CN@BTO composite samples with different g-C$_3$N$_4$ mass fractions were prepared (i.e., 5%CN@BTO, 10%CN@BTO, and 15%CN@BTO).

Fabrication of CN@Au@BTO Composites

CN@Au@BTO composites were prepared using the following two processes: The first process was to decorate Au nanoparticles on the surface of g-C$_3$N$_4$

nanosheets via a photocatalytic reduction route. Stoichiometric ammonium oxalate (AO, 0.025 g) and g-C_3N_4 nanosheets (0.13 g) were placed in deionized water (80 mL), followed by ultrasonic dispersion (30 min) and magnetic stirring (1 h). Subsequently, $HAuCl_4$ aqueous solution (0.029 mol L^{-1}, 1 mL) was added to the above suspension, followed by irradiation using a 15-W low-pressure mercury lamp for 30 min. The product, i.e., CN@Au composite, was rinsed with deionized water/absolute ethanol and subjected to drying at 60°C for 12 h. In the second step, the as-prepared CN@Au composite was loaded in the precursor mixture solution that was used for preparation of $Bi_4Ti_3O_{12}$ nanosheets as described in "Synthesis of g-C_3N_4 and $Bi_4Ti_3O_{12}$ Nanosheets" section. The subsequent hydrothermal treatment process followed the same procedure as used for the $Bi_4Ti_3O_{12}$ preparation. The composite derived according to this procedure is denoted as 10%CN@4.2%Au@BTO, where g-C_3N_4 and Au had a mass fraction of $\sim$ 10% and $\sim$ 4.2%, respectively. Figure 1 depicts the preparation process for the CN@BTO and CN@Au@BTO composite photocatalysts.

Sample Characterization Methods

X-ray powder diffraction (XRD) analysis was carried out using a D8 Advance x-ray diffractometer ($\lambda_{Cu\text{-}K\alpha}$ = 0.15406 nm). A TU-1901 double-beam spectrophotometer was applied for ultraviolet–visible (UV–Vis) diffuse reflectance spectroscopy (DRS). Fourier-transform infrared (FTIR) spectra were collected using a Spectrum Two FTIR spectrophotometer. A JSM-6701F field-emission scanning electron microscope was employed for scanning electron microscopy (SEM) observations. Transmission electron microscopy (TEM) investigations were carried out by means of a JEM-1200EX field-emission

transmission electron microscope. X-ray photoelectron spectroscopy (XPS) was carried out on a PHI-5702 multifunctional x-ray photoelectron spectrometer.

Photocatalytic Testing Process

Simulated-sunlight-driven photodecomposition of RhB was used to evaluate the photoactivity of the as-prepared photocatalysts. The initial RhB concentration was C_0 = 5 mg L^{-1}, and the photocatalyst dose was $C_{photocatalyst}$ = 1000 mg L^{-1}. The photoreactor (capacity 200 mL) was filled with 100 mL RhB solution together with 100 mg photocatalyst. The adsorption experiment was performed by placing the photoreactor in the dark for 30 min, during which magnetic stirring was applied. Thereafter, the light (a 200-W xenon lamp emitting simulated sunlight) was turned on to start the photocatalytic experiment. The variation of the RhB concentration during the photocatalysis was determined by testing the absorbance at λ_{RhB} = 554 nm using a UV–Vis spectrophotometer. The photocatalyst was removed from the reaction solution by centrifugation to test the absorbance of the reaction solution. Based on the initial concentration (C_0) and residual concentration (C_t) of RhB, the degradation percentage (η) of RhB was derived as: $\eta = (C_0 - C_t)/C_0 \times 100\%$.

RESULTS AND DISCUSSION

The XRD patterns of g-C_3N_4, $Bi_4Ti_3O_{12}$, and 10%CN@4.2%Au@BTO were recorded to determine their crystalline structure and are shown in Fig. 2. In the XRD pattern of g-C_3N_4, two diffraction peaks were observed at 13.17° and 27.40°, corresponding to the in-plane structural packing motif of tri-s-triazine units, i.e., (100) facet, and the interlayer stacking of conjugated aromatic system, i.e., (002)
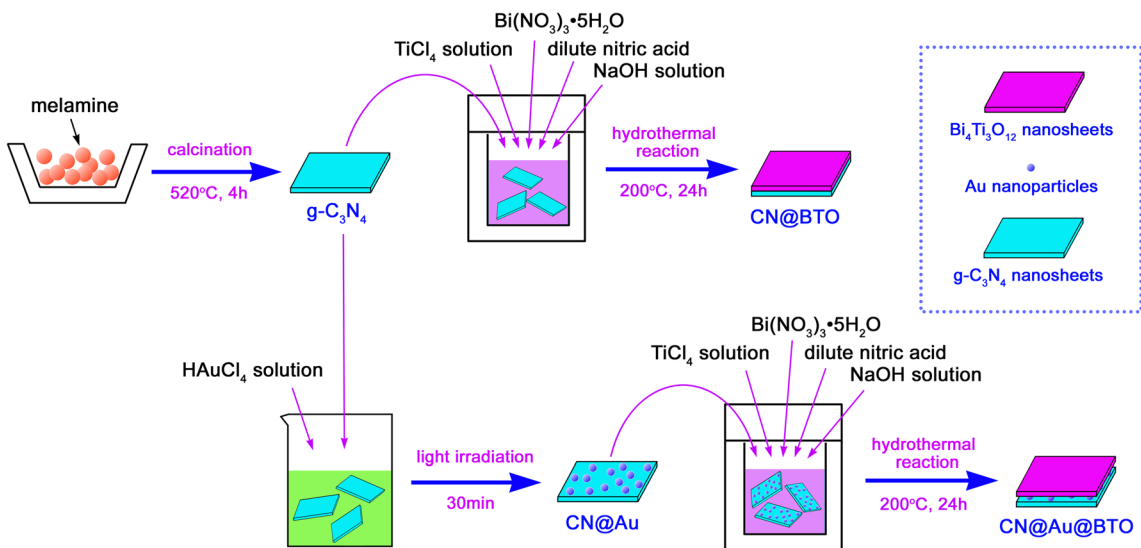

Fig. 1. Schematic of preparation processes of CN@BTO and CN@Au@BTO composite photocatalysts

facet, respectively.[47] This diffraction features suggest that g-C$_3$N$_4$ nanosheets were obtained. The diffraction peaks of Bi$_4$Ti$_3$O$_{12}$, matching well with the data in PDF#35-0795, imply the formation of pure Bi$_4$Ti$_3$O$_{12}$ in orthorhombic phase (cell dimensions 0.545 nm × 3.282 nm × 0.541 nm). The XRD pattern of 10%CN@4.2%Au@BTO was very similar to that of bare Bi$_4$Ti$_3$O$_{12}$, indicating no structural change of the orthorhombic Bi$_4$Ti$_3$O$_{12}$ in the composite. The XRD pattern of the composite presented no diffraction peaks assignable to g-C$_3$N$_4$ nanosheets or Au nanoparticles, which may be due to the low diffraction intensities of g-C$_3$N$_4$ and low content of Au.

It is necessary to characterize the light absorption characteristics of nanomaterials because they are strongly related to their physical properties.[48–50] UV–Vis DRS measurements were carried out to determine the optical absorption properties of Bi$_4$Ti$_3$O$_{12}$, g-C$_3$N$_4$, 10%CN@BTO, and 10%CN@4.2%Au@BTO. As shown in Fig. 3a, Bi$_4$Ti$_3$O$_{12}$, g-C$_3$N$_4$, and 10%CN@BTO exhibited poor visible-light absorption in the wavelength region $\lambda > 450$ nm. In contrast, the 10%CN@4.2%Au@BTO composite with the introduction of Au nanoparticles manifested relatively higher visible-light absorption, which can be attributed to the strong light absorption of Au nanoparticles in the visible-light region. The absorption peak observed at around 550 nm for the 10%CN@4.2%Au@BTO composite can be characterized as the plasmon resonance peak of Au nanoparticles.[35] Figure 3c shows the apparent colors of the samples, further confirming their visible-light absorption properties. It is observed that Bi$_4$Ti$_3$O$_{12}$, g-C$_3$N$_4$, and 10%CN@BTO presented a white or faint-yellow color, implying weak visible-light absorption by these samples. In contrast, a gray color was observed for 10%CN@4.2%Au@BTO, suggesting relatively stronger visible-light absorption
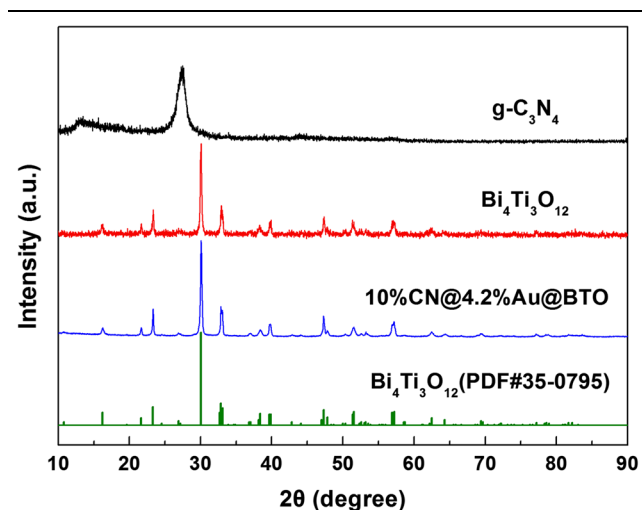

Fig. 2. XRD patterns of g-C$_3$N$_4$, Bi$_4$Ti$_3$O$_{12}$, and 10%CN@4.2%Au@BTO.
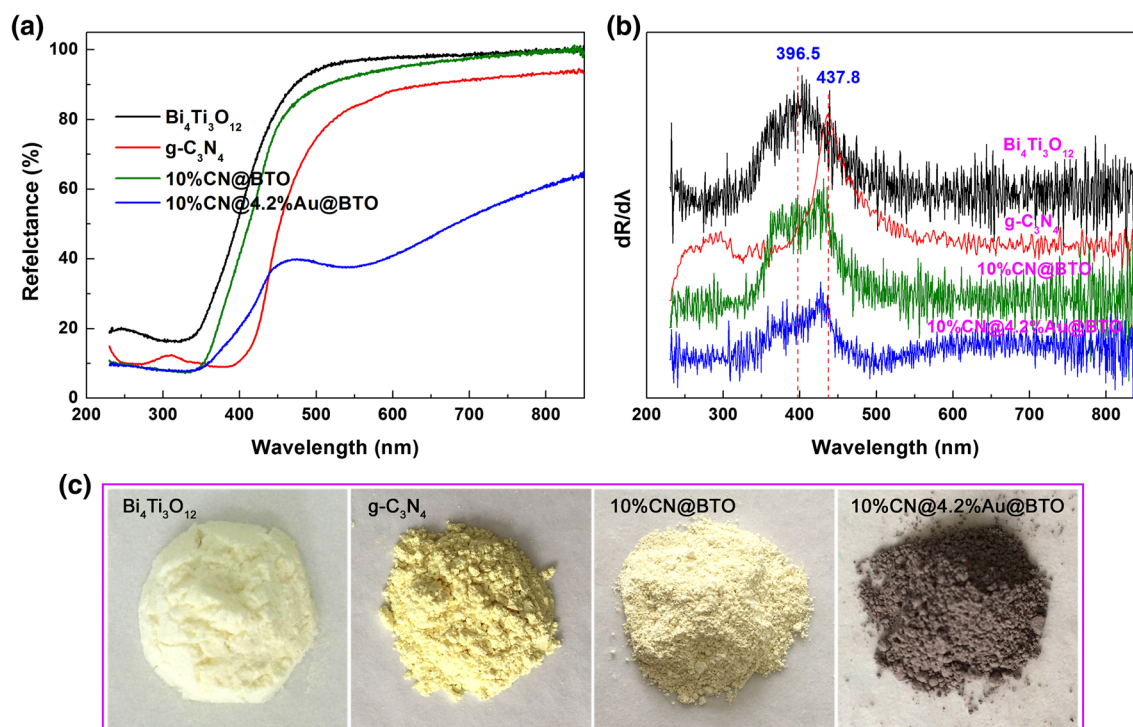

Fig. 3. (a) UV–Vis DRS spectra, (b) corresponding differential curves, and (c) apparent colors of Bi$_4$Ti$_3$O$_{12}$, g-C$_3$N$_4$, 10%CN@BTO, and 10%CN@4.2%Au@BTO
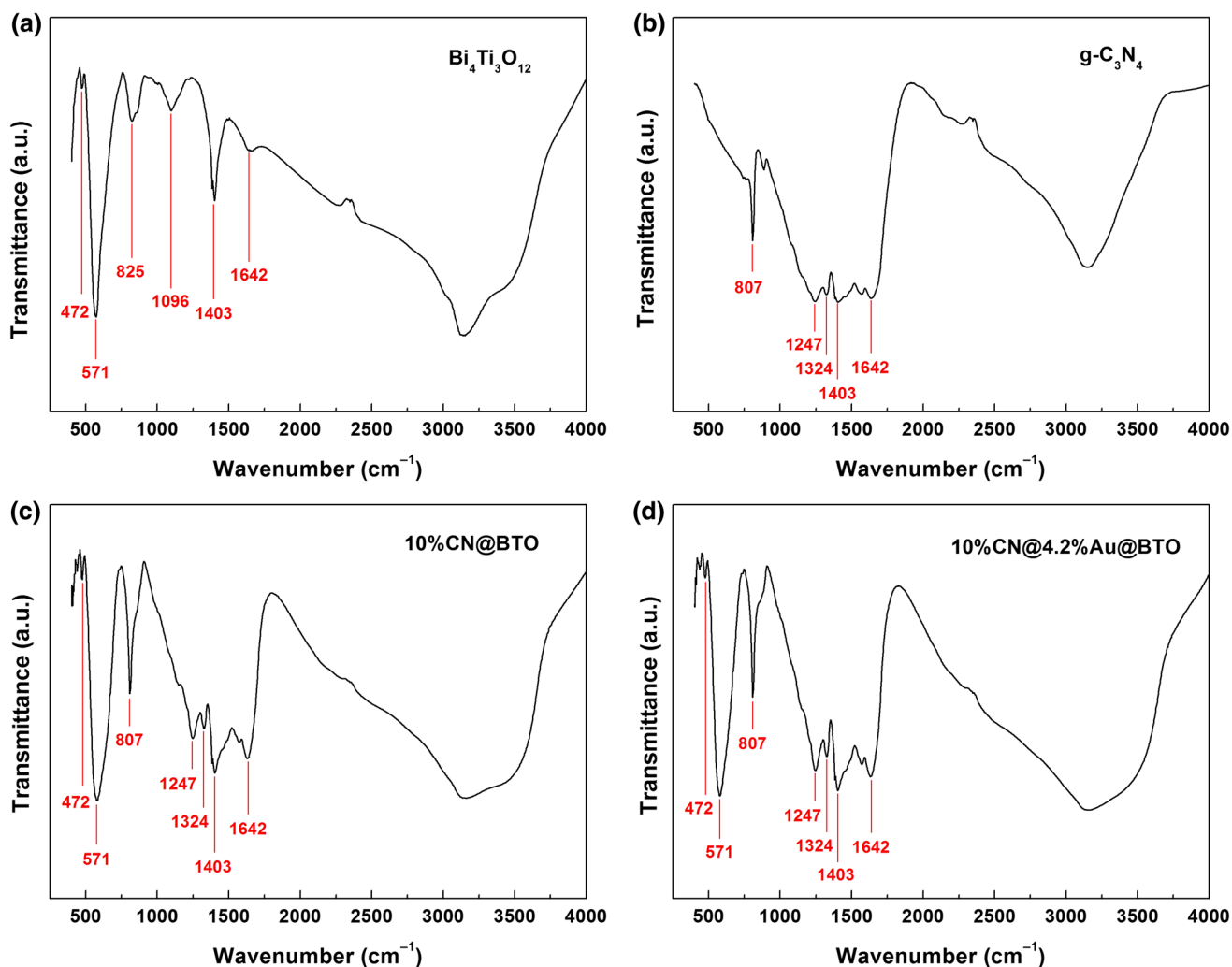
Fig. 4. FTIR spectra of $Bi_4Ti_3O_{12}$ (a), g-C_3N_4 (b), 10%CN@BTO (c), and 10%CN@4.2%Au@BTO (d)

of the ternary composite photocatalyst. Figure 3b depicts the differential UV–Vis DRS curves, from which the wavelength of the absorption edge (λ_{abs}) can be derived.[51] The bandgap of bare $Bi_4Ti_3O_{12}$ and g-C_3N_4 was thus obtained as 3.13 eV and 2.83 eV, respectively. For the 10%CN@BTO and 10%CN@4.2%Au@BTO composites, the bandgap of $Bi_4Ti_3O_{12}$ and g-C_3N_4 underwent a slight change, possibly due to their interaction.

FTIR spectroscopy was employed to study the possible presence of functional groups in the samples, as illustrated in Fig. 4. Figure 4a shows the FTIR spectrum of $Bi_4Ti_3O_{12}$, where the absorption peaks located at 571 cm^{-1} and 472 cm^{-1} originate from stretching vibration of Ti–O, and the peak at 825 cm^{-1} is ascribed to Bi–O stretching vibration, confirming the crystallization of the $Bi_4Ti_3O_{12}$ structure.[35] The peaks at 1096 cm^{-1} and 1403 cm^{-1} could originate from the symmetric and antisymmetric stretching vibrations of CO_3^{2-} groups introduced onto the surface of $Bi_4Ti_3O_{12}$ during the hydrothermal synthesis process, respectively.[52] The absorption peak observed at 1642 cm^{-1} was induced

by H–O bending vibration of water molecules.[53] In the FTIR spectrum of g-C_3N_4 (Fig. 4b), the characteristic absorption peaks of g-C_3N_4 nanosheets were observed at 807 cm^{-1} (breathing mode of tri-s-triazine units), 1247 cm^{-1}/1324 cm^{-1} (stretching vibrations of C–NH–C bridges), and 1410 cm^{-1} to 1640 cm^{-1} (C–N heterocycle skeletal vibrations of aromatic rings).[47] For the 10%CN@BTO and 10%CN@4.2%Au@BTO composites, the absorption peaks of $Bi_4Ti_3O_{12}$ and g-C_3N_4 were detected in their FTIR spectra (Fig. 4c, d), indicating that $Bi_4Ti_3O_{12}$ and g-C_3N_4 were included in the composites without structural change. No peaks characteristic of Au nanoparticles were detected for 10%CN@4.2%Au@BTO, possible due to the infrared inactivity of Au nanoparticles. For all the samples, the presence of CO_3^{2-} groups and water molecules on their surface was confirmed by the observation of infrared absorption peaks at 1403 cm^{-1} and 1642 cm^{-1}.

SEM observations were carried out to study the morphology of $Bi_4Ti_3O_{12}$ and 10%CN@4.2%Au@BTO. Figure 5a shows a SEM

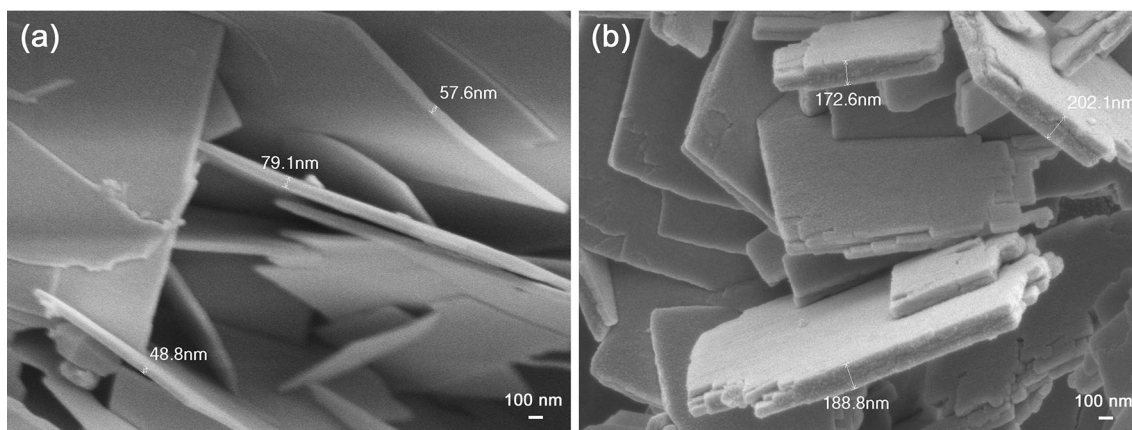Fig. 5. SEM images of (a) Bi$_4$Ti$_3$O$_{12}$ and (b) 10%CN@4.2%Au@BTO
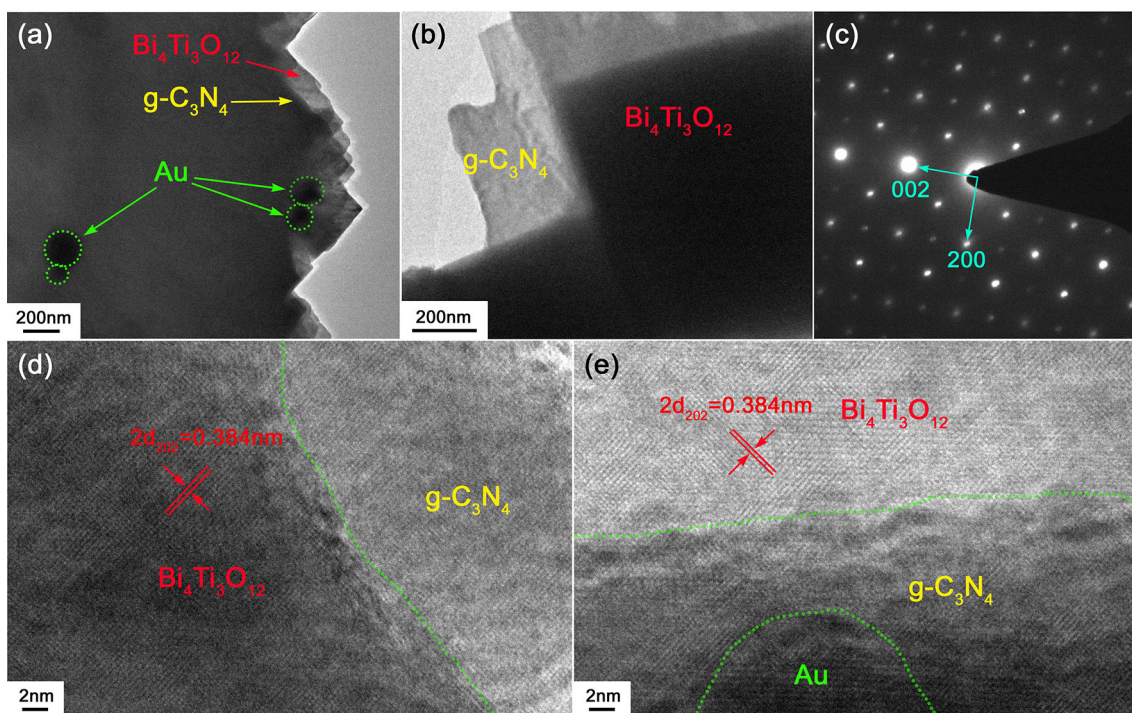
Fig. 6. TEM images (a,b), SAED pattern (c), and HRTEM images (d,e) of 10%CN@4.2%Au@BTO

image of Bi$_4$Ti$_3$O$_{12}$, indicating that Bi$_4$Ti$_3$O$_{12}$ crystallized as nanosheets with thickness of 45 nm to 80 nm (average thickness $\sim$ 60 nm). The surface of the Bi$_4$Ti$_3$O$_{12}$ nanosheets appeared to be smooth and clean. Figure 5b shows a SEM image of 10%CN@4.2%Au@BTO, demonstrating the formation of composite nanosheets with thickness of 150 nm to 210 nm (average thickness $\sim$ 170 nm). Compared with that of the bare Bi$_4$Ti$_3$O$_{12}$ nanosheets, the thickness of the composite nanosheets was greatly increased, suggesting that they were constructed by g-C$_3$N$_4$ and Bi$_4$Ti$_3$O$_{12}$ nanosheets with face-to-face contact. Moreover, the surface of the composite nanosheets became rough, possibly due to decoration by Au nanoparticles.

To reveal the microstructure of the 10%CN@4.2%Au@BTO composite, TEM investigation was further performed. Figure 6a and b shows TEM images of the composite, demonstrating that g-C$_3$N$_4$ nanosheets and Bi$_4$Ti$_3$O$_{12}$ nanosheets were coupled face-to-face, with Au nanoparticles possibly sandwiched between them. The selected-area electron diffraction (SAED) pattern in Fig. 6c shows periodically arranged diffraction spots that can be indexed to the [010] zone axis of Bi$_4$Ti$_3$O$_{12}$ orthorhombic phase. This implies that the Bi$_4$Ti$_3$O$_{12}$ nanosheets had single-crystalline nature with highly exposed (010) facet. No diffraction spots or rings from g-C$_3$N$_4$ nanosheets and Au nanoparticles were detected in the SAED pattern, possibly due to
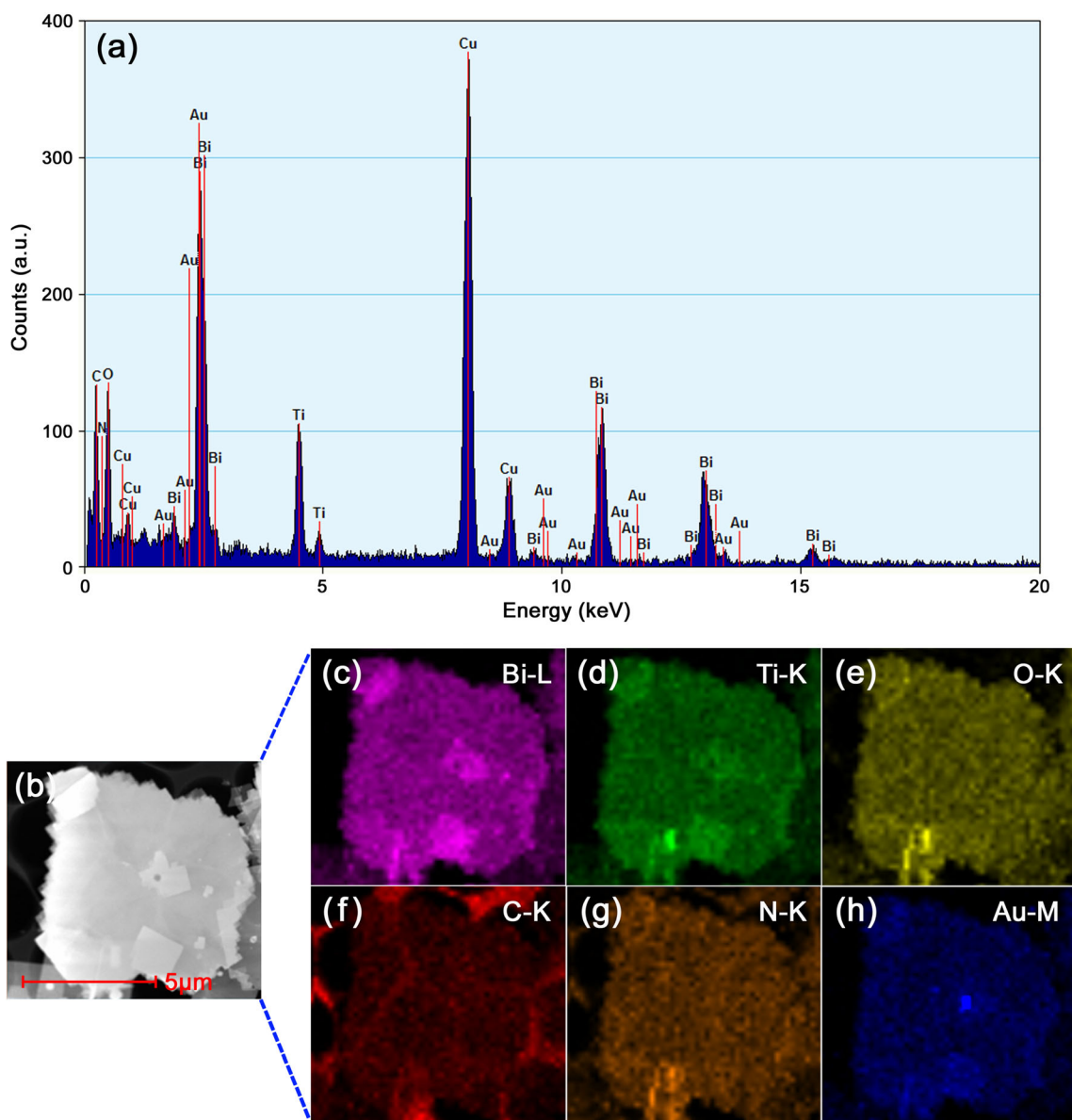
Fig. 7. EDS spectrum (a), DF-STEM image (b), and EDS elemental mapping images (c–h) of 10%CN@4.2%Au@BTO

the amorphous nature of g-C_3N_4 nanosheets and absence of Au nanoparticles from the selected area. Figure 6d and e show high-resolution TEM (HRTEM) images of the composite, further elucidating the construction of 2D-g-C_3N_4@0D-Au@2D-$Bi_4Ti_3O_{12}$ heterojunctions with face-to-face contact. The clear lattice fringes at $2d$ = 0.384 nm, corresponding to the (202) facet of orthorhombic $Bi_4Ti_3O_{12}$, confirm the single-crystalline nature of $Bi_4Ti_3O_{12}$ nanosheets with highly exposed (010) facet.

The energy-dispersive x-ray spectroscopy (EDS) spectrum obtained from the 10%CN@4.2%Au@BTO composite (Fig. 7a) clearly confirmed the presence of C, N, O, Bi, Ti, O, and Au species in the composite. Except for the Cu signals, possibly resulting from the TEM microgrid holder,[54] no other impurity

elements were detected in the EDS spectrum. Figure 7b shows a dark-field scanning TEM (DF-STEM) image recorded from 10%CN@4.2% Au@BTO, while the corresponding EDS elemental maps of the area are presented in Fig. 7c, d, e, f, and h. It is obvious that the composite nanosheets exhibited a uniform distribution of C, N, O, Bi, Ti, and O elements, whereas Au element was dispersedly decorated on the composite nanosheets. These results of the elemental mapping analysis support the construction of 2D/0D/2D face-to-face contact g-C_3N_4@Au@$Bi_4Ti_3O_{12}$ heterojunctions.

The 10%CN@4.2%Au@BTO composite was analyzed by XPS to study the chemical states of the elements Bi, Ti, O, C, N, and Au in the composite, as shown in Fig. 8. Two separate peaks with binding energy of 159.1 eV (Bi $4f_{7/2}$) and 164.4 eV (Bi $4f_{5/2}$)
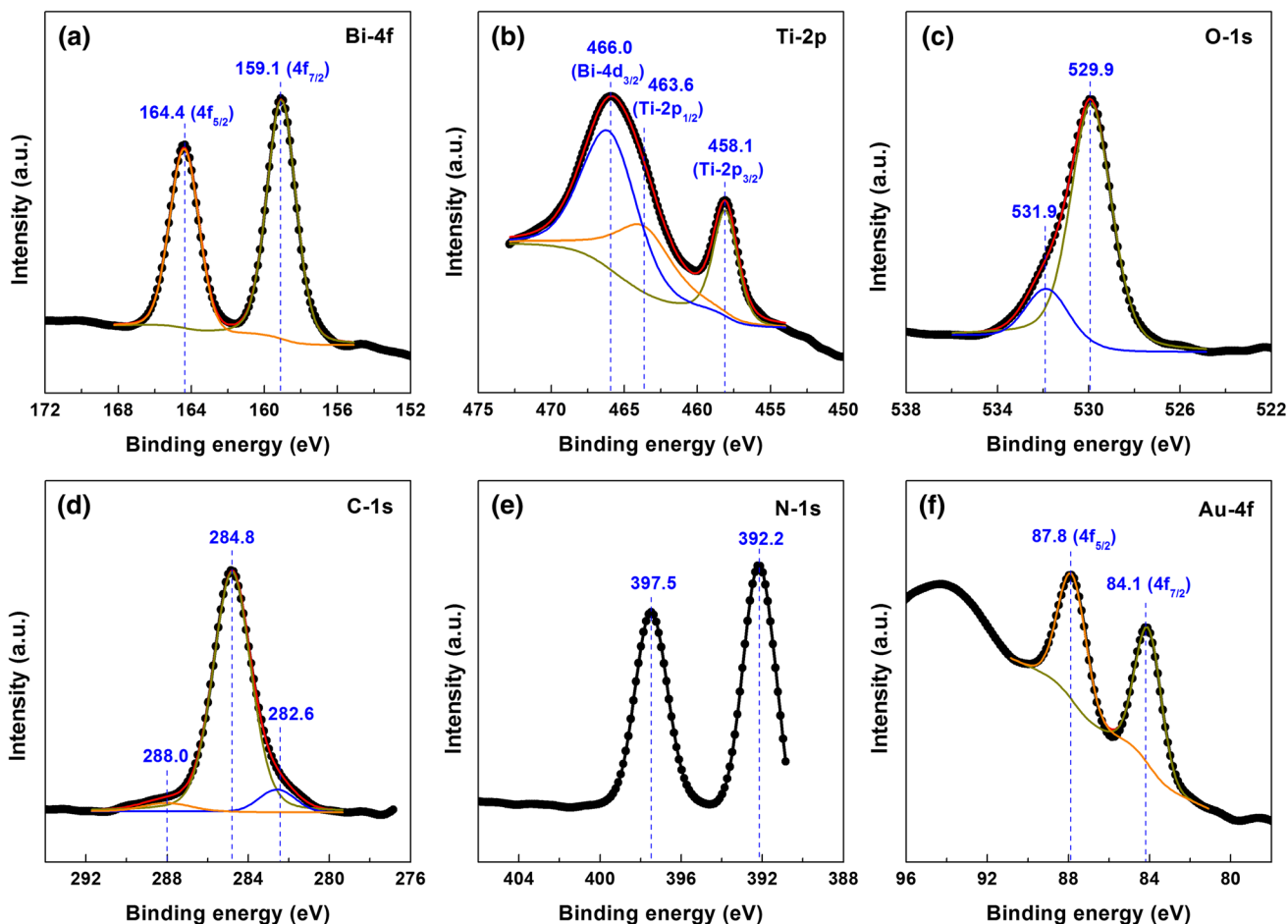
Construction of 2D/0D/2D Face-to-Face Contact g-C$_3$N$_4$@Au@Bi$_4$Ti$_3$O$_{12}$ Heterojunction
Photocatalysts for Degradation of Rhodamine B
5255

Fig. 8. High-resolution XPS spectra of (a) Bi $4f$, (b) Ti $2p$, (c) O $1s$, (d) C $1s$, (e) N $1s$, and (f) Au $4f$ of 10%CN@4.2%Au@BTO

were observed in the Bi $4f$ core-level XPS spectrum (Fig. 8a), implying the presence of Bi^{3+} oxidation state.[35,55] Deconvolution of the Ti $2p$ core-level XPS spectrum (Fig. 8b) revealed three peaks at 458.1 eV, 463.6 eV, and 466.0 eV. The former two peaks correspond to the binding energies of Ti^{4+} $2p_{3/2}$ and Ti^{4+} $2p_{1/2}$, respectively, whereas the third peak can be attributed to the binding energy of Bi $4d_{3/2}$.[35,56] The O $1s$ XPS spectrum (Fig. 8c) revealed two kinds of oxygen species, i.e., crystal lattice oxygen of Bi$_4$Ti$_3$O$_{12}$ (529.9 eV) and chemisorbed oxygen species on the sample (531.9 eV).[35,57,58] The C $1s$ XPS spectrum (Fig. 8d) showed three peaks located at 284.8 eV, 288.0 eV, and 282.6 eV, which are characteristic of carbon present in the instrument, sp^2-hybridized carbon in g-C$_3$N$_4$, and metal carbides, respectively.[47] In the N $1s$ XPS spectrum (Fig. 8e), the binding energy peak at 397.5 eV can be ascribed to sp^2-hybridized nitrogen (C=N–C) resulting from g-C$_3$N$_4$.[47] The strong peak at 392.2 eV can be ascribed to formation of metal nitrides. The signals observed at binding energies of 84.1 eV (Au $4f_{7/2}$) and 87.8 eV (Au $4f_{5/2}$) in the Au $4f$ XPS spectrum

(Fig. 8f) are indicative of the presence of metallic Au nanoparticles in the composite.[35]

Figure 9a shows the time-dependent degradation curves of RhB as photocatalyzed by Bi$_4$Ti$_3$O$_{12}$, g-C$_3$N$_4$, CN@BTO composites, and 10%CN@4.2%Au@BTO composite. Before photocatalysis, the dye adsorption onto the samples was determined to be 5.4% to 9.9%. The blank (photolysis) experiment showed that RhB exhibited good stability under simulated sunlight irradiation in the absence of photocatalysts.[59] Under irradiation for 120 min, bare Bi$_4$Ti$_3$O$_{12}$ and g-C$_3$N$_4$ photocatalyzed 71.0% and 44.8% degradation of RhB, respectively. When Bi$_4$Ti$_3$O$_{12}$ nanosheets and g-C$_3$N$_4$ nanosheets were coupled face-to-face, the resulting CN@BTO composite nanosheets exhibited improved photodecomposition performance. The 10%CN@BTO composite with g-C$_3$N$_4$ mass fraction of 10% was shown to be the optimal composite photocatalyst, achieving a RhB degradation percentage of 85.3% after 120 min photoreaction. Furthermore, by sandwiching Au nanoparticles between the Bi$_4$Ti$_3$O$_{12}$ and g-C$_3$N$_4$ nanosheets, the more promising ternary
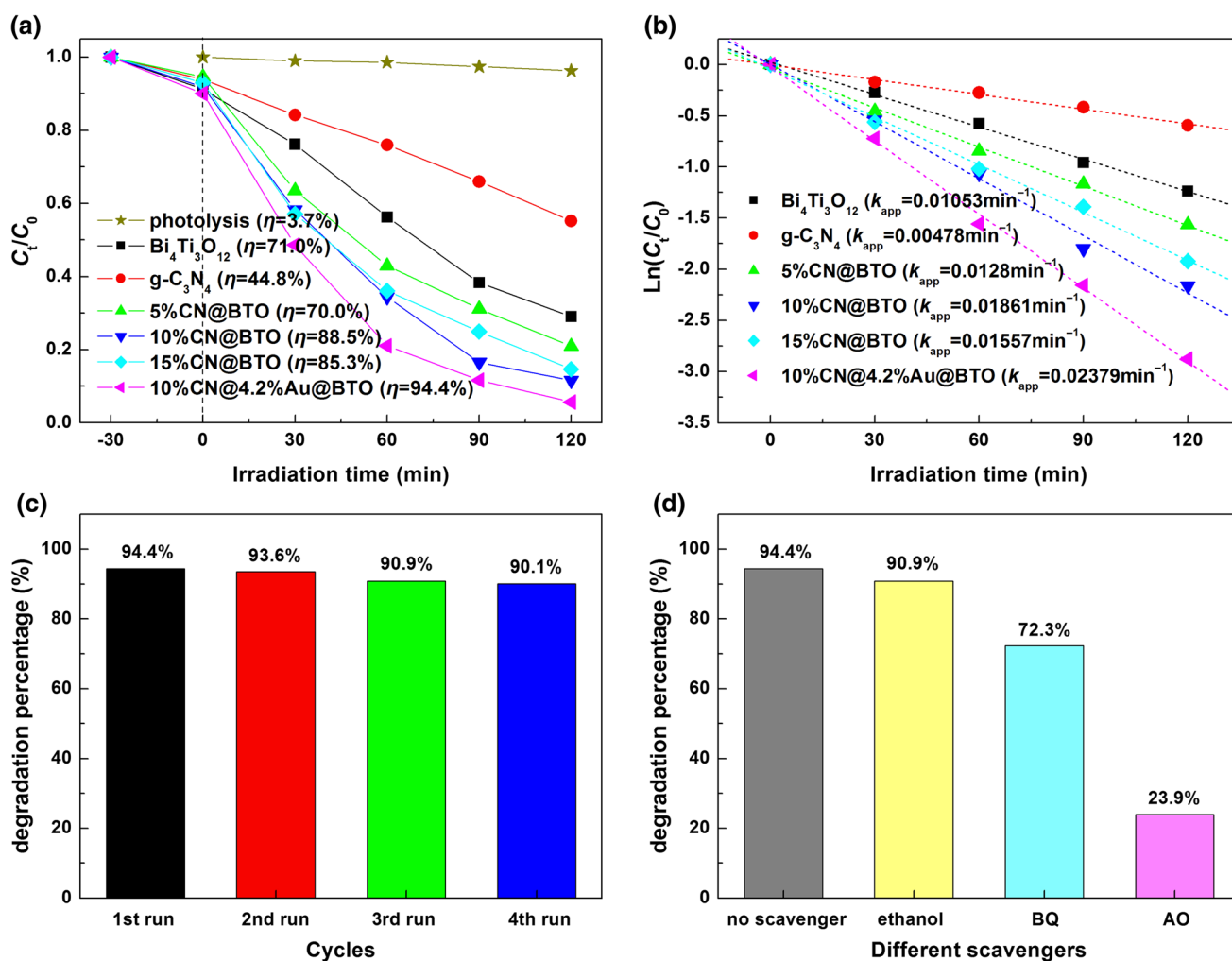
Fig. 9. (a) Photodegradation plots of RhB as photocatalyzed by all the samples. (b) RhB degradation kinetic plots. (c) Photodegradation percentage of RhB during repeated use of 10%CN@4.2%Au@BTO. (d) Effects of ethanol, BQ, and AO on RhB degradation percentage over 10%CN@4.2%Au@BTO

10%CN@4.2%Au@BTO composite photocatalyst was obtained, resulting in photodegradation of 94.4% of RhB.

The photodegradation performance of the samples was further elucidated from the kinetic viewpoint. As shown in Fig. 9b, the degradation kinetic plots of RhB conformed perfectly to the pseudo-first-order kinetic equation $Ln(C_t/C_0) = -k_{app}t$,[60,61] exhibiting good linear behavior with R^2 values above 0.99. The apparent first-order reaction rate constant k_{app} can be used for quantitative comparison of the photodegradation performance of the photocatalysts. According to the values of k_{app} shown in Fig. 9b, it can be concluded that the 10%CN@BTO composite exhibited photodegradation activity that was ~ 1.8 and ~ 3.9 times greater than that of bare $Bi_4Ti_3O_{12}$ and g-C_3N_4, respectively, whereas the photodegradation activity of the ternary 10%CN@4.2%Au@BTO was 2.3 and 5.0 greater compared with that of bare $Bi_4Ti_3O_{12}$ and g-C_3N_4, respectively.

To examine the reusability of 10%CN@4.2% Au@BTO for photocatalytic degradation of RhB,

the photocatalyst was collected by centrifugation after the photodegradation experiment and recovered by rinsing with deionized water. The next photodegradation experiment was carried out using the same procedure by loading the recovered 10%CN@4.2%Au@BTO into fresh RhB solution. To balance the minor loss of photocatalyst after each run, fresh photocatalyst was added. As shown in Fig. 9c, the photodegradation percentage of RhB within the 120 min reaction decreased slightly from 94.4% in the first cycle to 90.1% in the fourth cycle, implying that the degradation percentage of RhB underwent only a minor loss (3.3%). The results of this recycling photocatalytic experiment clearly demonstrate the excellent stability of the 10%CN@4.2%Au@BTO composite photocatalyst for repeated degradation of organic dyes.

In the 10%CN@4.2%Au@BTO photodegradation system, the active species including hydroxyl (·OH) radicals, superoxide (·O$_2^-$) radicals, and photoexcited holes were determined by active species trapping experiments as described in literature.[62] Ethanol
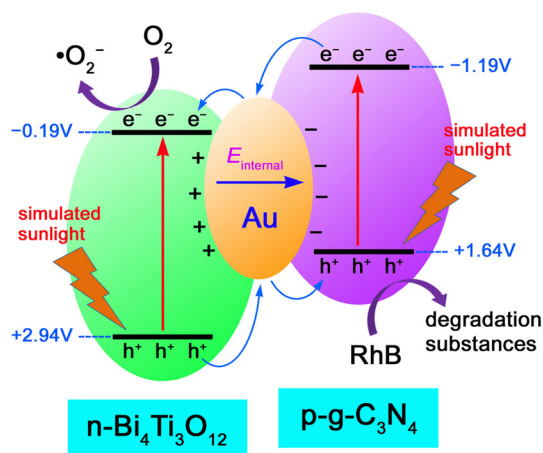
Fig. 10. Schematic of photocatalytic mechanism of *g*-C₃N₄@Au@Bi₄Ti₃O₁₂ heterojunction photocatalysts

(scavenger for ·OH, 5 mL), benzoquinone (BQ, scavenger for ·O_2^-, 0.1 mmol), and ammonium oxalate (AO, scavenger for h⁺, 0.1 mmol) were added separately to the photoreaction solution to examine their effect on the RhB degradation. As shown in Fig. 9d, addition of ethanol had only a minor effect on the photodegradation of RhB, suggesting a very small role for ·OH in the photodegradation process. However, the dye degradation was obviously inhibited by the introduction of BQ or AO, confirming that ·O_2^- and h⁺ are the main reactive species causing the dye degradation. In particular, photoexcited h⁺ plays the greatest role in the photocatalysis, as indicated by the highest suppression efficiency of AO. To quantitatively determine the role of the reactive species in the photodegradation process, trapping experiments using more quenchers would be necessary.[63]

Note that Bi₄Ti₃O₁₂ is an intrinsic *n*-type semiconductor (E_g = 3.13 eV) while *g*-C₃N₄ behaves as an intrinsic *p*-type semiconductor (E_g = 2.83 eV).[35] The CB/VB potentials of Bi₄Ti₃O₁₂ and *g*-C₃N₄ were theoretically estimated using the method elaborated in literature[64,65] to be −0.19/+2.94 V and −1.19/+1.64 V versus normal hydrogen electrode (NHE), respectively, as depicted schematically in Fig. 10. When Bi₄Ti₃O₁₂ nanosheets, Au nanoparticles, and *g*-C₃N₄ nanosheets are coupled to form 2D/0D/2D face-to-face contact CN@Au@BTO heterojunctions, electrons will diffuse from *n*-type Bi₄Ti₃O₁₂ to *p*-type *g*-C₃N₄, while conversely, holes will diffuse from *p*-type *g*-C₃N₄ to *n*-type Bi₄Ti₃O₁₂. The role of the Au nanoparticles sandwiched between the Bi₄Ti₃O₁₂ and *g*-C₃N₄ nanosheets is to act as a "bridge" to facilitate such transfer of photoexcited carriers. This carrier diffusion process leads to the creation of negative charge centers at the *g*-C₃N₄ interface and positive charge centers at the Bi₄Ti₃O₁₂ interface, with the simultaneous formation of an internal electric field (pointing from Bi₄Ti₃O₁₂ to *g*-C₃N₄). The creation of this internal electric field will prevent the continuous diffusion of

the charge carriers, and finally a thermal equilibrium state will be reached in the CN@Au@BTO heterojunction. Under irradiation by simulated sunlight, both Bi₄Ti₃O₁₂ and *g*-C₃N₄ are photoexcited to generate electrons in the CB and holes in the VB. The internal electric field then drives electron migration from the *g*-C₃N₄ CB to Bi₄Ti₃O₁₂ CB, while conversely hole migration from the Bi₄Ti₃O₁₂ VB to the *g*-C₃N₄ VB occurs, using the Au nanoparticles as the "bridge." This thereby results in efficient separation of photogenerated electrons and holes, as confirmed by photocurrent and photoelectrochemical impedance spectroscopy (EIS) analyses (Supplementary Figs. S1 and S2). As a result, more electrons accumulate in the CB of Bi₄Ti₃O₁₂ while holes accumulate in the VB of *g*-C₃N₄ and are expected to participate in the photoreactions. This is the major factor resulting in the enhanced photocatalytic performance of the ternary CN@Au@BTO heterojunction composite photocatalysts. Moreover, other secondary factors could also cause dye degradation. For example, the LSPR of the Au nanoparticles could result in local electromagnetic field enhancement and thus stimulate production of additional electrons/holes in Bi₄Ti₃O₁₂ and *g*-C₃N₄, and LSPR-induced electrons in the Au nanoparticles could also take part in the photoreactions.

As the main reactive species confirmed in the CN@Au@BTO photocatalytic system, ·O_2^- radicals can be thermodynamically generated via the reaction between CB electrons in Bi₄Ti₃O₁₂ with adsorbed O₂ species, since the Bi₄Ti₃O₁₂ CB potential (−0.19 V versus NHE) is negative with respect to the O_2/·O_2^- redox potential (−0.13 V versus NHE[66]). From the thermodynamic viewpoint, holes in the *g*-C₃N₄ VB cannot combine with OH⁻ or H₂O species to form ·OH radicals, because the *g*-C₃N₄ VB potential (+1.64 V versus NHE) is not sufficiently positive when compared with E^0(OH⁻/·OH) = +1.99 V or E^0(H₂O/·OH) = +2.38 V versus NHE.[67] Direct oxidation by photoexcited h⁺ is suggested as another important mechanism causing the dye degradation, which agrees with the results of the active species trapping experiments.

CONCLUSIONS

By coupling Bi₄Ti₃O₁₂ and *g*-C₃N₄ nanosheets face-to-face and sandwiching Au nanoparticles between them, 2D/0D/2D face-to-face contact *g*-C₃N₄@Au@Bi₄Ti₃O₁₂ heterojunction photocatalysts were prepared. Photocatalytic experiments suggested that the as-prepared ternary composite photocatalysts exhibited good activity for photocatalytic degradation of RhB under simulated sunlight irradiation. After 120 min of photoreaction, the 10%CN@4.2%Au@BTO composite photocatalyst demonstrated photocatalytic degradation of 94.4% of RhB. Kinetic analysis revealed its photodegradation activity to be about 2.3 and 5.0 times greater

than that of bare $Bi_4Ti_3O_{12}$ and g-C_3N_4 nanosheets, respectively. The mechanism underlying this enhanced photodegradation of the ternary composite photocatalysts is mainly attributed to transfer of photoexcited electrons/holes between $Bi_4Ti_3O_{12}$ and g-C_3N_4 nanosheets and efficient spatial separation of electron–hole pairs. The role of the Au nanoparticles sandwiched between the $Bi_4Ti_3O_{12}$ and g-C_3N_4 nanosheets is to act as a "bridge" to facilitate such carrier transfer.

ACKNOWLEDGEMENTS

ELECTRONIC SUPPLEMENTARY MATERIAL

The online version of this article (https://doi.org/10.1007/s11664-020-08243-2) contains supplementary material, which is available to authorized users.

REFERENCES

1. Y.X. Yan, H. Yang, Z. Yi, and T. Xian, *Catalysts* 9, 795 (2019).
2. S. Wang, C. Chen, Y. Li, Q. Zhang, Y. Li, and H. Gao, *J. Electron. Mater.* 48, 6675 (2019).
3. Z.M. He, B. Tang, J.B. Su, and Y.M. Xia, *J. Mater. Sci. Mater. Electron.* 29, 19544 (2018).
4. M. Kumari and A.K. Saroha, *J. Environ. Manag.* 228, 169 (2018).
5. Y.X. Yan, H. Yang, Z. Yi, T. Xian, R.S. Li, and X.X. Wang, *Desalin. Water Treat.* 170, 349 (2019).
6. S.F. Wang, H.J. Gao, Y. Wei, Y.W. Li, X.H. Yang, L.M. Fang, and L. Lei, *CrystEngComm* 21, 263 (2019).
7. Z. Yi, X. Li, H. Wu, X.F. Chen, H. Yang, Y.J. Tang, Y.G. Yi, J.Q. Wang, and P.H. Wu, *Nanomaterials* 9, 1254 (2019).
8. Y.M. Xia, Z.M. He, J.B. Su, S.Q. Zhu, and B. Tang, *J. Electron. Mater.* (2020). https://doi.org/10.1007/s11664-020-08022-z.
9. S.Y. Wang, H. Yang, Z. Yi, and X.X. Wang, *J. Environ. Manag.* 248, 109341 (2019).
10. M. Ahmadi, H.R. Motlagh, N. Jaafarzadeh, A. Mostoufi, R. Saeedi, G. Barzegar, and S. Jorfi, *J. Environ. Manag.* 186, 55 (2017).
11. C. Cai, S.B. Han, W. Liu, K. Sun, L. Qiao, S. Li, and X.T. Zu, *Appl. Catal. B Environ.* 260, 118103 (2020).
12. S.P. Huang, Z.Q. Wei, X.J. Wu, and J.W. Shi, *Mater. Res. Express* 7, 015025 (2020).
13. Z.Y. Pang, H. Tong, X.X. Wu, J.K. Zhu, X.X. Wang, H. Yang, and Y.P. Qi, *Opt. Quant. Electron.* 50, 335 (2018).
14. H. Tong, Y.Q. Xu, Y.W. Su, and X.X. Wang, *Res. Phys.* 14, 102460 (2019).
15. X.X. Wang, Z.Y. Pang, H. Yang, and Y.P. Qi, *Res. Phys.* 14, 102446 (2019).
16. C.L. Cen, Z.Q. Chen, D.Y. Xu, L.Y. Jiang, X.F. Chen, Z. Yi, P.H. Wu, G.F. Li, and Y.G. Yi, *Nanomaterials* 10, 95 (2020).
17. C.L. Cen, Y.B. Zhang, X.F. Chen, H. Yang, Z. Yi, W.T. Yao, Y.J. Tang, Y.G. Yi, J.Q. Wang, and P.H. Wu, *Physica E* 117, 113840 (2020).
18. J.K. Li, X.F. Chen, Z. Yi, H. Yang, Y.J. Tang, Y. Yi, W.T. Yao, J.Q. Wang, and Y.G. Yi, *Mater. Today Energy* 16, 100390 (2020).
19. J.K. Li, Z.Q. Chen, H. Yang, Z. Yi, X.F. Chen, W.T. Yao, T. Duan, P.H. Wu, G.F. Li, and Y.G. Yi, *Nanomaterials* 10, 257 (2020).
20. S.B. Han, Y.M. Zhu, C. Cai, J.K. Zhu, W.B. Han, L. Chen, X.T. Zu, H. Yang, and M. Gu, *Appl. Phys. Lett.* 114, 113901 (2019).
21. F.A. Zhao, H.Y. Xiao, X.M. Bai, and X.T. Zu, *Phys. Chem. Chem. Phys.* 21, 16108 (2019).
22. Y.P. Wang, H. Yang, X.F. Sun, H.M. Zhang, and T. Xian, *Mater. Res. Bull.* 124, 110754 (2020).
23. A. Esmaeili and M.H. Entezari, *J. Colloid Interface Sci.* 466, 227 (2016).
24. L.J. Di, T. Xian, X.F. Sun, H.Q. Li, Y.J. Zhou, J. Ma, and H. Yang, *Micromachines* 10, 503 (2019).
25. H. Huan, H.G. Jile, Y.J. Tang, X. Li, Z. Yi, X. Gao, X.F. Chen, J. Chen, and P.H. Wu, *Micromachines* 11, 309 (2020).
26. T. Xian, L.J. Di, X.F. Sun, H.Q. Li, Y.J. Zhou, and H. Yang, *Nanoscale Res. Lett.* 14, 397 (2019).
27. T. Xian, X.F. Sun, L.J. Di, Y.J. Zhou, J. Ma, H.Q. Li, and H. Yang, *Catalysts* 9, 1031 (2019).
28. A.S. Jonathan, L.K. Ai, and A.D. Jennifer, *Nature* 483, 421 (2012).
29. X.X. Wang, J.K. Zhu, H. Tong, X.D. Yang, X.X. Wu, Z.Y. Pang, H. Yang, and Y.Y. Qi, *Chin. Phys. B* 28, 044201 (2019).
30. F. Qin, Z.Q. Chen, X.F. Chen, Z. Yi, W.T. Yao, T. Duan, P.H. Wu, H. Yang, G.F. Li, and Y.G. Yi, *Nanomaterials* 10, 207 (2020).
31. Z.M. He, Y.M. Xia, and J.B. Su, *RSC Adv.* 8, 39187 (2018).
32. S.T. Guan, H. Yang, X.F. Sun, and T. Xian, *Opt. Mater.* 100, 109644 (2020).
33. Q.Q. Duan, J.Y. Jia, X. Hong, Y.C. Fu, C.Y. Wang, K. Zhou, X.Q. Liu, H. Yang, and Z.Y. Wang, *Sol. Energy* 201, 555 (2020).
34. C. Cai, Y. Mi, S.B. Han, Q. Wang, W. Liu, X.Q. Wu, Z. Zheng, X. Xia, L. Qiao, W.L. Zhou, and X.T. Zu, *Electrochim. Acta* 295, 92 (2019).
35. H. Wu, H. Jile, Z. Chen, D. Xu, Z. Yi, X. Chen, J. Chen, W. Yao, P. Wu, and Y. Yi, *Micromachines* 11, 189 (2020).
36. X.X. Zhao, H. Yang, Z.M. Cui, Z. Yi, and H. Yu, *J. Mater. Sci. Mater. Electron.* 30, 13785 (2019).
37. Z.W. Chen, H. Jiang, W.L. Jin, and C.K. Shi, *Appl. Catal. B Environ.* 180, 698 (2016).
38. D.P. Dutta and A.K. Tyagi, *Mater. Res. Bull.* 74, 397 (2016).
39. G. Odling, E. Chatzisymeon, and N. Robertson, *Catal. Sci. Technol.* 8, 829 (2018).
40. C.X. Zheng, H. Yang, Z.M. Cui, H.M. Zhang, and X.X. Wang, *Nanoscale Res. Lett.* 12, 608 (2017).
41. K. Das, D. Majhi, Y.P. Bhoi, and B.G. Mishra, *Chem. Eng. J.* 362, 588 (2019).
42. S.E. Cummins and L.E. Cross, *J. Appl. Phys.* 39, 2268 (1968).
43. X. Wang, K. Maeda, A. Thomas, K. Takanabe, G. Xin, J.M. Carlsson, K. Domen, and M. Antonietti, *Nat. Mater.* 8, 76 (2009).
44. Y. Guo, J.H. Li, Z.Q. Gao, X. Zhu, Y. Liu, Z.B. Wei, W. Zhao, and C. Sun, *Appl. Catal. B Environ.* 192, 57 (2016).
45. L.J. Di, H. Yang, T. Xian, and X.J. Chen, *Micromachines* 9, 613 (2018).
46. R. Mohini and N. Lakshminarasimhan, *Mater. Res. Bull.* 76, 370 (2016).
47. Y.X. Yan, H. Yang, Z. Yi, R.S. Li, and T. Xian, *Solid State Sci.* 100, 106102 (2020).
48. Y.Y. Wang, Z.Q. Chen, D.Y. Xu, Z. Yi, X.F. Chen, J. Chen, Y.J. Tang, P.H. Wu, G.F. Li, and Y.G. Yi, *Res. Phys.* 16, 102951 (2020).
49. J. Pu, G.P. Li, Q.Q. Jiang, and X.T. Zu, *Chin. Phys. C* 44, 014001 (2020).
50. J. Chen, X.X. Wang, F. Tang, X. Ye, L.M. Yang, and Y.B. Zhang, *Res. Phys.* 16, 102867 (2020).
51. Y.X. Yan, H. Yang, Z. Yi, T. Xian, and X.X. Wang, *Environ. Sci. Pollut. Res.* 26, 29020 (2019).
52. S. Utara and S. Hunpratub, *Ultrason. Sonochem.* 41, 441 (2018).

Construction of 2D/0D/2D Face-to-Face Contact g-C$_3$N$_4$@Au@Bi$_4$Ti$_3$O$_{12}$ Heterojunction
Photocatalysts for Degradation of Rhodamine B

5259

53. S. Wang, H. Gao, Y. Wang, G. Sun, X. Zhao, H. Liu, C. Chen, and L. Yang, *J. Electron. Mater.* (2020). https://doi.org/10.1007/s11664-020-07941-1.
54. S. Wang, H. Gao, C. Chen, Q. Li, C. Li, Y. Wei, and L. Fang, *J. Mater. Sci. Mater. Electron.* 30, 15744 (2019).
55. O. Dehghani Dastjerdi, H. Shokrollahi, and H. Yang, *Ceram. Int.* 46, 2709 (2020).
56. Z. Yi, Y. Zeng, H. Wu, X.F. Chen, Y.X. Fan, H. Yang, Y.J. Tang, Y.G. Yi, J.Q. Wang, and P.H. Wu, *Res. Phys.* 15, 102609 (2019).
57. M. Golkari, H. Shokrollahi, and H. Yang, *Ceram. Int.* 46, 8553 (2020).
58. S. Wang, H. Gao, G. Sun, Y. Li, Y. Wang, H. Liu, C. Chen, and L. Yang, *Opt. Mater.* 99, 109562 (2020).
59. H.J. Gao, C.X. Zheng, H. Yang, X.W. Niu, and S.F. Wang, *Micromachines* 10, 557 (2019).
60. W.H. Zhao, Z.Q. Wei, X.D. Zhang, M.J. Ding, and S.P. Huang, *Mater. Res. Bull.* 124, 110749 (2020).
61. Y.M. Xia, Z.M. He, Y.L. Lu, B. Tang, S.P. Sun, J.B. Su, and X.P. Li, *RSC Adv.* 8, 5441 (2018).
62. Y.C. Ye, H. Yang, H.M. Zhang, and J.L. Jiang, *Environ. Technol.* 41, 1486 (2020).
63. J. Rivas, R.R. Solis, O. Gimeno, and J. Sagasti, *Int. J. Environ. Sci. Technol.* 12, 513 (2015).
64. S. Wang, H. Gao, C. Chen, Y. Wei, and X. Zhao, *J. Sol-Gel. Sci. Technol.* 92, 186 (2019).
65. T. Andersen, H.K. Haugen, and H. Hotop, *J. Phys. Chem. Ref. Data* 28, 1511 (1999).
66. Y.P. Wang, F.C. Jiang, J.F. Chen, X.F. Sun, T. Xian, and H. Yang, *Nanomaterials* 10, 178 (2020).
67. Y.X. Yan, H. Yang, Z. Yi, X.X. Wang, R.S. Li, and T. Xian, *Environ. Eng. Sci.* 37, 64 (2020).